




Research article

# Correlation between solution relative viscosity and the microstructural properties of the poly(3-hydroxybutyrate-co-3-hydroxyvalerate) – PHBV solution blow spun mats

Lucas Gomes Rabello<sup>1,2</sup>, Maira Rievers Nogueira Alvares<sup>1</sup>,  
Roberto Carlos da Conceição Ribeiro<sup>2</sup>, Paula Mendes Jardim<sup>1</sup>,  
Rossana Mara da Silva Moreira Thiré<sup>1\*</sup>

<sup>1</sup>Program of Metallurgical and Materials Engineering – PEMM/COPPE, Universidade Federal do Rio de Janeiro – UFRJ, 21941-598, Rio de Janeiro, Brazil

<sup>2</sup>Centre of Mineral Technology – CETEM, 21941-908, Rio de Janeiro, Brazil

Received 28 May 2023; accepted in revised form 12 September 2023

**Abstract.** In this study, we produced poly(3-hydroxybutyrate-co-3-hydroxyvalerate) (PHBV) fibrous mats via solution blow spinning (SBS) and evaluated their microstructural properties. We propose here the utilization of the theoretical estimative of relative viscosity ( $RV$ ) as an independent variable in a statistical design of experiments (DoE) to account for the polymer's molecular weight ( $M_w$ ) effect on the determination of the diameter and morphology of the fibers. The  $RV$  of the solution ( $42.3 \cdot 10^3$ – $287.4 \cdot 10^3$ ) and air pressure –  $AP$  (70–140 kPa) were varied. The analysis of variance (ANOVA) indicated that the increase in  $RV$  favored an increment in fiber size and resistance to alignment. Higher  $AP$  produced aligned and thinner fibers with higher crystallinity. The spinnability regions were determined based on the estimated  $RV$  of the PHBV solutions and the  $AP$  levels. Fibers were formed at 70 kPa from solutions with  $RV$  ranging from  $10 \cdot 10^3$  to  $10^6$ , while at 140 kPa, from  $42 \cdot 10^3$  to  $10^6$ . Nanofibers were produced from less viscous solutions ( $RV = 42.3 \cdot 10^3$ – $124.4 \cdot 10^3$ ), while microfibers were produced from solutions with  $RV = 287.4 \cdot 10^3$ . The developed ANOVA model predicted with good accuracy ( $R_{adj}^2 = 0.96$ ) the average diameter of the PHBV fibers produced from the SBS technique using polymers with distinct  $M_w$  values, including those available in the literature data.

**Keywords:** poly(hydroxy alkanoates), solution blow spinning (SBS), micro-and nanofibers, design of experiments, relative viscosity

## 1. Introduction

Polymeric micro- and nanostructured fibers capable of superior interfacial interaction within their working environment have been gaining prominence worldwide in applications such as sensing devices [1–3], air filtering [4–7], wastewater treatment [8–10], fiber-reinforced plastics [11, 12], protective clothing [13–15], and tissue engineering [16–27] due to their high surface area/volume ratio. In this sense, scientists

aware of this tendency must consider the critical need to reduce plastic waste production while selecting these materials by developing new sustainable polymers and aiming for manufacturing techniques that make them widely accessible. Under such a scenario, biodegradable biopolyesters are a creative and intelligent solution to tackle the human urge for sustainable polymeric materials and plastic waste environment pressure [28–30].

\*Corresponding author, e-mail: [rossana@metalmat.ufrj.br](mailto:rossana@metalmat.ufrj.br)

© BME-PT

Poly(3-hydroxybutyrate-*co*-3-hydroxyvalerate) – PHBV is one of the most promising biodegradable polyesters to replace petroleum-based plastics in terms of performance and reduction of plastic environmental impact. PHBV is considered environmentally friendly because of its microbiological origins, biodegradability, and null toxicity [31]. Additionally, it has a significant advantage over other polymers since it can be produced from waste materials and does not promote soil acidification and water eutrophication, like starch and corn-based biopolymers [32]. Consisting of a linear chain with randomly distributed methyl and ethyl side groups [30–40], PHBV has better processability than other hard-to-process poly(hydroxy alkanates) (PHA) and mechanical properties similar to those of high-density polyethylene (HDPE) and polypropylene (PP) [28–35, 40–42]. Besides, it has well-established applications in the manufacture of drug delivery systems [19, 34], bioabsorbable surgical sutures [19], biodegradable implants [19], biosensors [19], porous scaffolds [36–38], and food packaging [19, 41]. However, since its processability in the molten state is still inferior to those from fossil-based polymers, the referred PHA constitutes a small portion of the world's bioplastics production capacity [28, 29]. In this sense, wet-processing techniques involving polymeric solutions, such as electrospinning [16], bubble electrospinning [43], centrifugal spinning [44], and solution blow spinning (SBS) [16, 21], have garnered significant research interest for their potential to expand the polymer fiber's production capacity.

Electrospinning, for example, is a widely utilized method that employs a high electric field to draw a polymer solution into ultrafine fibers. While it offers the advantage of producing homogeneous nanometer-sized fibers, it suffers from low production rates and high energy costs, limiting its suitability for large-scale applications [16, 21]. Bubble electrospinning was developed as an alternative approach to address the production rate limitations by utilizing multiple bubbles as simultaneous fiber-drawing elements. However, despite its potential, bubble electrospinning still faces challenges in terms of high production costs associated with the demanded energy [43]. Centrifugal spinning, on the other hand, does not require high voltages since it utilizes centrifugal force to stretch and eject the polymer solution into fibers, offering higher efficiency compared to the previous methods. However, it does lack precise control over

fiber diameter [44]. In contrast, SBS has gained attention for its potential to achieve high productivity and energy efficiency. This method involves forcing a polymer solution through a nozzle while subjecting it to a high-speed gas stream as the driving force for the fiber formation. Moreover, its integration into continuous manufacturing processes makes it highly suitable for large-scale production. Consequently, SBS stands out as a promising alternative to other spinning techniques for the production of micro- and nanostructured mats [45–49].

Several biodegradable polymers, such as polylactic acid (PLA) [22, 50, 51], polycaprolactone (PCL) [20], polybutylene succinate (PBS) [52], and cellulose [21], have been used to produce micro- and nanofibrous non-woven mats. However, since SBS's advent in 2009 [53], only two papers have studied producing fibers from PHBV solutions, being of our group [54]. Souza *et al.* [55] presented a controlled release system of sodium diclofenac through drug encapsulation in PHBV nanofibers, while Carlos *et al.* [54] evaluated PLA and PHBV fiber mats via SBS encapsulating a bioactive agent system. However, these studies did not provide relevant statistical evidence to verify the influence of the processing variables on the PHBV fibers' morphology and diameter, nor did they account for the fact that distinct  $M_w$  values from the same polymer can result in drastic variations in the fibrous mats' characteristics, implying low reproducibility and application restrictions to the spun material. For example, Srinivasan *et al.* [56] produced beads on string fibers of PMMA using a weight average molecular weight  $M_w = 761 \cdot 10^3 \text{ g} \cdot \text{mol}^{-1}$  polymer. However, the same solution concentration was not spinnable at the same processing conditions when an  $M_w = 272 \cdot 10^3 \text{ g} \cdot \text{mol}^{-1}$  PMMA was utilized.

In brief, solutions are only spinnable in the semi-dilute regime with concentrations values above the overlap concentration ( $c^*$ ). The latter can be estimated by Equation (1), where  $M_w$  is the polymer molecular weight,  $R_g$  is the radius of gyration, and  $N_a$  is the Avogadro's number. Above this concentration, the polymer coils begin to entangle, increasing the solution viscosity and possibly allowing fiber formation [48, 49]. Notably, from Equation (1),  $c^*$  is not a unique value for a certain polymer/solvent system since it depends on the  $M_w$ . Thus, solutions of a high-molecular-weight polymer in general, have a lower  $c^*$  than a low-molecular-weight one,

as previously discussed by Srinivasan *et al.* [56] (Equation (1)):

$$c^* = \frac{3M_w}{4\pi R_g^3 N_a} \quad (1)$$

In contrast with the previous paragraph discussion, works have shown DoE studies for diameter and morphology prediction using the solution concentration as a processing variable of the SBS technique, not accounting for the polymer  $M_w$  effect [46, 47]. Even though these studies have found a good prediction capacity over the response variables, their results are restricted to a specific value of  $M_w$ , such as shown in the work of Srinivasan *et al.* [56], and do not solve the reproducibility problem of the spun biopolymers from natural sources.

According to Gupta *et al.* [57], the effect of the polymer concentration and  $M_w$  on the spinnability of semi-dilute solution of linear polymers are two faces of the same coin, called viscosity. These terms relate to the  $RV$  by the power law function shown in Equation (2), where  $\eta_s$  is the solvent zero-shear viscosity,  $\eta$  is the solution's zero-shear viscosity, and  $v$  is the Flory exponent (0.6 for good solvents). The authors also observed a strong correlation between the fiber's diameter and the relative viscosity ( $RV$ ) utilizing this power law dependence for the electrospinning technique. Hence, adopting the  $RV$  as a processing variable in a DoE instead of the solution concentration seems a promising approach to predict the SBS-fiber diameter and solve the low reproducibility problem that biopolymers have (Equation (2)):

$$RV = \frac{\eta}{\eta_s} = \left(\frac{c}{c^*}\right)^{\frac{3}{3v-1}} = \left(\frac{c}{c^*}\right)^{3.75} \quad (2)$$

In this sense, this study presents the generation of PHBV fibrous mats via SBS and its evaluation supported by a DoE to effectively contribute to a more efficient SBS process for producing reproducible micro- and nanofibers from PHBV. Here, we present a mathematical model developed by the experimental data collected in DoE using the  $RV$  and  $AP$  as processing variables to predict the fibers' diameter in semi-dilute solutions. In addition, the influence of these variables was also investigated on the fiber orientation and crystallinity. The same solvent (chloroform) within the same processing conditions as in the work of Carlos *et al.* [54] was used but with distinct polymer concentrations and  $M_w$  to evaluate the

model accuracy for the PHBV-spun material with the literature data.

## 2. Experimental section / methods

### 2.1. Materials

Samples were produced using PHBV with a 3-hydroxyvalerate (3HV) content of 2% [30], in powder form (ENMAT PHBV Resin Y1000P, TianAn Biologic Materials Co., Ningbo, China), gently supplied by Technische Universität Chemnitz, Germany. Chloroform stabilized with amylene (C2432), 99.5% purity, was purchased from Sigma-Aldrich, São Paulo, SP, Brazil.

### 2.2. Gel permeation chromatography (GPC)

The  $M_w$  were determined by gel permeation chromatography (GPC) with a Malvern Viscotek GPCmax chromatograph (Malvern, United Kingdom) equipped with three columns (Shodex GPC HFIP803, Shodex GPC HFIP-804 and Shodex GPC HFIP-805, Showa Denko, Tokyo, Japan). The analyses were performed in  $3 \text{ mg}\cdot\text{ml}^{-1}$  solutions using hexafluoroisopropanol (HFIP) as solvent at  $40^\circ\text{C}$  and with a constant solvent flow rate of  $1.0 \text{ ml}\cdot\text{min}^{-1}$ . A calibration curve was constructed with poly(methyl methacrylate) standards (American Polymer Standards, Mentor, USA).

### 2.3. Fiber production

The SBS system consisted of an air compressor supplied by Schulz (Joinville, Brazil), an analog manometer to adjust the air pressure, an injection pump (BSV 700 Flex Pump) provided by Biosensor (Americana, Brazil) coupled to a 12 ml syringe, an adapted injection device from core-shell fiber production containing co-axial needles [54], and a solid-static collector. Initially, the solutions of 3, 4, and 5%  $m/V$  were prepared by solubilizing the PHBV ( $M_w = 953 \cdot 10^3 \text{ g}\cdot\text{mol}^{-1}$ ) powder in chloroform under vigorous stirring at  $60^\circ\text{C}$ . Then, these were submitted to the spinning process using a distance from a static collector of 30 cm and with the same parameter used by Carlos *et al.* [54] but spun at 70 and 140 kPa.

### 2.4. Scanning electron microscopy (SEM)

The morphological analysis of PHBV fiber mats was performed by the SEM images obtained in a Hitachi TM3030Plus (Hitachi, Tokyo, Japan) equipment with a secondary electron detector (SED) at 15 kV. The fiber diameter was measured using the software

ImageJ, according to the procedure presented by Bortolassi *et al.* [58], with a minimum of 100 measurements for each SEM image. In addition, the fibers' orientation distribution was studied following Carlos *et al.* [54]. Finally, the alignment index ( $AI$  [%]) was calculated based on the method proposed by Sun *et al.* [59], utilizing, for each image analyzed, the vector field generated in the ImageJ plugin OrientationJ [60]. This method allows quantifying the fiber alignment through an index ( $AI$ ) that ranges from 0 (for totally random fibers) to 100 (for totally aligned fibers) [59].

Three SEM images ( $n = 3$ ) taken from different regions of a mat produced from a single experimental condition were evaluated to statistically represent the fibrous material's average fiber diameter and orientation [54, 58]. In the case of fiber diameter, more than 300 measurements were performed on a single fibrous mat. Additionally, ANOVA occurred utilizing the calculated average values of diameter and  $AI$  for each image (in triplicate) to increase the statistical accuracy of the estimated effects.

## 2.5. Schlieren's visualization method

The role of  $AP$  in fiber morphology was investigated using Schlieren's visualization method. This method allows for visualizing and evaluating the airflow profile as it leaves the injection device at different pressures and inferring how it affects the fiber morphology [61]. Figure 1 shows the test apparatus consisting of a point-light source, a biconvex lens of 10 cm in diameter, a thin razor positioned at twice the focal distance ( $f$ ), and a Sony Cyber-Shot DSC-HX100V (Sony, Tokyo, Japan) camera to capture the images. The emitted light gets refracted from its rectilinear path when the airflow passes between the lens and

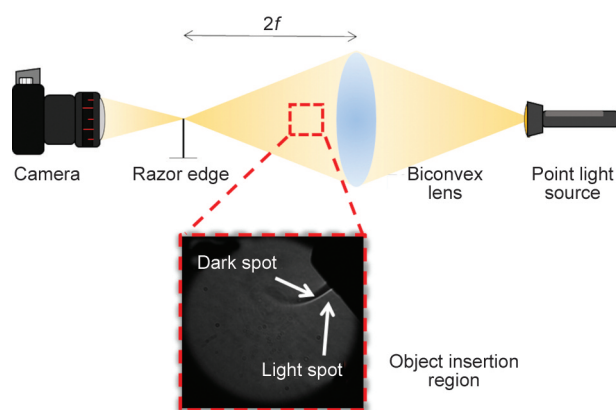


**Figure 1.** Schlieren's visualization apparatus for the airflow behavior acquisition.

the razor. If the deviation is large enough, as for the low-density regions in the airflow profile with a low refractive index, the razor blocks the light, forming dark zones in the image [61, 62]. The dashed red square in Figure 1 shows the test performed with an aerosol emitter, where light and dark zones can be seen, related to higher and lower air density regions in the aerosol flow, respectively.

## 2.6. X-ray diffraction (XRD)

The crystallographic analysis of PHBV mats was carried out in a SHIMADZU XRD-6000 diffractometer (Shimadzu, Kyoto, Japan), using  $\text{CuK}\alpha$  radiation (30 kV/ 30 mA/  $\lambda = 1,542 \text{ \AA}$ ), scanning from  $2^\circ$  to  $50^\circ$  ( $2\theta$ ), goniometer speed of  $2^\circ \cdot \text{min}^{-1}$  and step of  $0.02^\circ$ . The sample's crystallinity index ( $CI$  [%]) was determined by Equation (3), where  $A_c$  is the integrated area under the diffraction peaks and  $A_a$  is the integrated area under the amorphous region [37]. Furthermore, the interplanar distance and the crystallite size associated with the (020) and (110) planes were measured from the X-ray diffractograms employing the same experimental procedure as Souza *et al.* [55] using the software OriginPro 8.5 (Origin Lab, USA) (Equation (3)):

$$CI [\%] = \frac{A_c}{A_c + A_a} \cdot 100 \quad (3)$$

## 2.7. Solutions relative viscosity ( $RV$ ) estimation

Equation (2) was employed to estimate the solution's  $RV$ . To do so, the overlap concentration ( $c^*$ ) values for each solution were calculated via Equation (1). Additionally, the radius of gyration ( $R_g$ ) of the PHBV molecule solubilized in chloroform was inferred by converting the measured  $M_w$  values according to the function proposed by Zagar and Kržan [63].

## 2.8. Statistical evaluation

The experimental data was collected using a mixed 2-and 3-level design to assess the impact of 3, 4, and 5%  $m/V$  PHBV ( $M_w = 953 \cdot 10^3 \text{ g} \cdot \text{mol}^{-1}$ ) solutions'  $RV$  (values estimated through Equation (1) and Equation (2)) and  $AP$  on diameter and alignment. In addition, a 2-level and 2-factor design was employed to investigate crystallinity. The statistical significance of the results was determined using analysis of variance (ANOVA) with a significance level of 5% ( $p$ -value  $< 0.05$ ) [64]. Table 1 presents the variables

**Table 1.** List of the process variables and their levels based on a mixed 2-and 3-level design.

Experimental conditions	SC <sup>a</sup> [% m/V]	Independent variables	
		RV <sup>b</sup> ( $\cdot 10^3$ )	AP <sup>c</sup> [kPa]
1	3	(-1) 2.3	(-1) 70
2	3	(-1) 42.3	(1) 140
3	4	(0) 124.5	(-1) 70
4	4	(0) 124.5	(1) 140
5	5	(1) 287.5	(-1) 70
6	5	(1) 287.5	(1) 140

<sup>a</sup>SC – PHBV solution concentration;  
<sup>b</sup>RV – PHBV solution relative viscosity;  
<sup>c</sup>AP – air pressure.

and their levels, where -1, 0, and 1 denote the lowest, central, and highest levels, respectively. All the analyses were performed in triplicate ( $n = 3$ ). The developed mathematical model for the fibers' average diameter prediction has the form shown in Equation (4) and was based on the diameter experimental results collected through the mixed 2-level and 3-level design used in this work. Where  $Y$  is the response variable,  $\beta_i$  ( $i = 0, 1, 2, 3, 4,$  and  $5$ ) are the regression coefficients calculated by the ANOVA,  $X_1$  and  $X_2$  are the 3-and 2-level independent variables, respectively, and  $\epsilon$  is the random error component [46]. In addition, test fibrous mats were produced using the same experimental procedure presented in the 'Fiber's production' section and had

their morphology and average diameter measured to validate the developed model. For this purpose, solutions with concentrations ranging from 1.5 to 9%  $m/V$  were prepared employing a PHBV with distinct  $M_w$  (501, 672, and 933  $10^3 \text{ g}\cdot\text{mol}^{-1}$ ) (Equation (4)):

$$Y = \beta_0 + \beta_1 \cdot X_1 + \beta_2 \cdot X_2 + \beta_3 \cdot X_1 \cdot X_2 + \beta_4 \cdot X_1^2 + \beta_5 \cdot X_2 \cdot X_1^2 + \epsilon \quad (4)$$

### 3. Results and discussion

#### 3.1. Injection device configuration and airflow behavior in the SBS technique

Figure 2a shows the SBS apparatus used in this study, along with the fibrous mats that adhered on the collector during production. In the SBS technique, the polymeric solution is expelled from the device as a jet and directed toward the collector by accelerated airflow [45, 48, 49]. When the airflow hits the static collector, it spreads radially, assisting the formation of fibers. Figure 2b displays photographs of the injection device's nozzles during the spinning process of the same polymeric solution, spun at 70 and 140 kPa, respectively. At lower spinning pressures, the jet appears to have a laminar flow, while a dispersive one with turbulent behavior is evident at higher pressures. The latter may hinder the polymer jet's stability, induce fiber formation with varying morphologies, and create a return flow [65, 66]. Atif *et al.* [66] suggested that the convergence

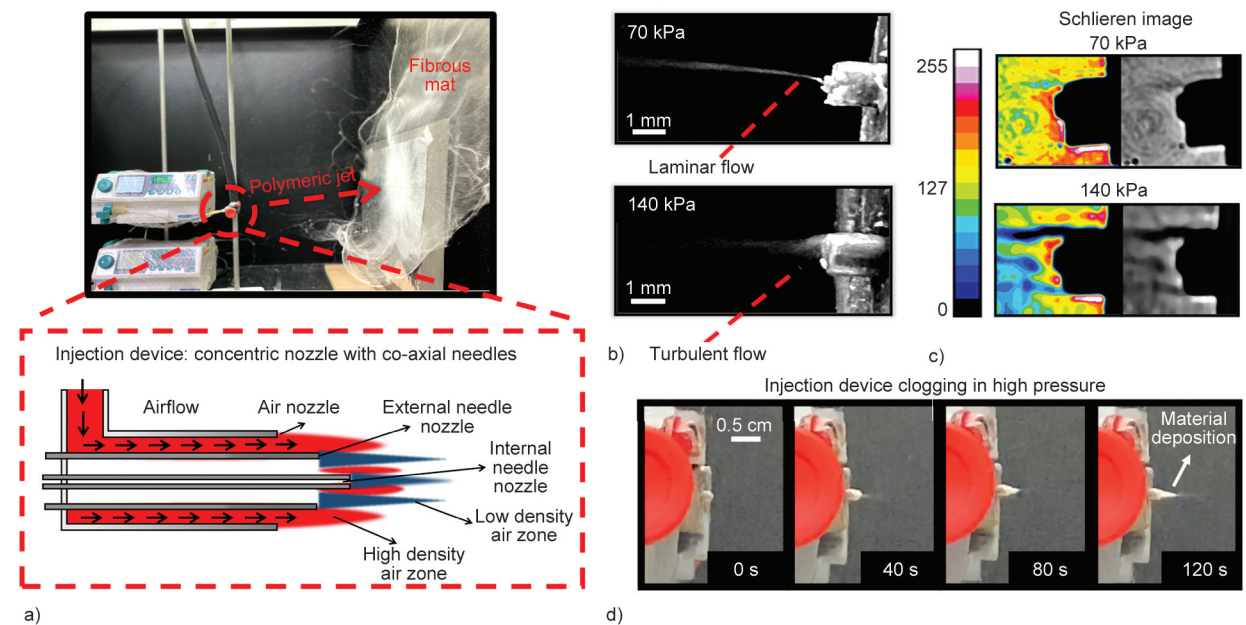


**Figure 2.** Airflow profile influence on the SBS technique: a) the SBS apparatus, the fibrous mats production, and injection device scheme; b) the polymeric jet near the nozzles photographed right after the spinning process started at 70 and 140 kPa; c) Schlieren's images of the nozzle tip at 70 and 140 kPa; d) material deposition and nozzle clogging.

of airflows in the low-pressure regions near the nozzles results in turbulence in the air motion, increasing in intensity with the released gas's velocity.

Figure 2c presents images obtained using Schlieren's method at the injection device's nozzle (right) without polymeric solution injection and with color filters (left) for enhanced visualization to support the previous discussion. It is possible to observe in Figure 2c lighter zones near the external and internal needle surfaces immediately after gas release, indicating denser air regions [61, 67]. Clearly,  $AP$  decreases significantly at the device's nozzles, creating dark, lower-density, triangular-shaped regions that cause airflow convergence to the nozzle, as predicted by Lou *et al.* [65]. This phenomenon allows the gas to increase its kinetic energy by conserving the energy lost by the drop in  $AP$ , generating the necessary driving force for solution ejection and polymer jet formation. However, contrary to what was reported by Lou *et al.* [65], up to three low-pressure zones were observed due to the injection device's configuration (adapted from a core-shell one) used in this work. The device has two concentric nozzles instead of one evaluated in the simulation presented by the authors. The low-density (dark) zones are more intense at pressures of 140 kPa than those of 70 kPa, which are difficult to observe with the adopted camera's resolution. For example, the injection device scheme shown in Figure 2a was created based on adapted literature simulations [65, 66], following the different density regions confirmed by the Schlieren images. This scheme clarifies the previous discussion by illustrating the opening for the air nozzle, the needles, and the airflow profile. Figure 2d evidences the return flow effect within the low-pressure zones at spinning pressures of 140 kPa. Notably, the needle's nozzle was entirely clogged in just 120 s due to the material deposition carried by the return flow, substantially reducing the SBS technique's productivity.

### 3.2. Processing parameters effect on the fiber morphology

Table 2 presents the estimated values of the radius of gyration ( $R_g$ ), overlap concentration ( $c^*$ ), and relative viscosity ( $RV$ ) for the solutions used in this work's DoE samples, the test samples, and the work by Carlos *et al.* [54]. The estimated  $RV$  values fall within the range of experimentally observed values for semi-dilute PHBV solutions in chloroform, as

**Table 2.** Estimate values of radius of gyration –  $R_g$  [nm], overlap concentration –  $c^*$  [%  $m/V$ ], and relative viscosity –  $RV$ .

$c^a$ [% $m/V$ ]	$R_g$ [nm]	$c^*$ [% $m/V$ ]	$c/c^*$	$RV$ ( $\cdot 10^3$ )
<b>This work design of experiment (DoE) samples (<math>M_w = 953 \cdot 10^3 \text{ g} \cdot \text{mol}^{-1}</math>)</b>				
3	60	0.17	17.13	42.3
4	60	0.17	22.84	124.4
5	60	0.17	28.55	287.4
<b>Test samples (<math>M_w = 953 \cdot 10^3 \text{ g} \cdot \text{mol}^{-1}</math>)</b>				
1.5	60	0.17	8.57	3.1
2	60	0.17	11.42	9.2
2.5	60	0.17	14.27	21.3
<b>Test samples (<math>M_w = 672 \cdot 10^3 \text{ g} \cdot \text{mol}^{-1}</math>)</b>				
3	46	0.27	10.94	7.8
4	46	0.27	14.59	23.1
5	46	0.27	18.24	53.5
6	46	0.27	21.88	106.0
7	46	0.27	25.53	189.0
8	46	0.27	29.18	311.8
9	46	0.27	40.27	1043.0
<b>Test samples (<math>M_w = 501 \cdot 10^3 \text{ g} \cdot \text{mol}^{-1}</math>)</b>				
4	43	0.25	15.98	3.2
6	43	0.25	23.98	149.3
8	43	0.25	31.97	439.3
<b>Carlos <i>et al.</i> [54] (<math>M_w = 170 \cdot 10^3 \text{ g} \cdot \text{mol}^{-1}</math>)</b>				
10	28	0.31	32.38	460.8

<sup>a</sup> $c$  – PHBV solution concentration.

reported by D'Haene *et al.* [68]. As expected, the results in Table 2 indicate that  $RV$  increases with the concentration of PHBV, which is associated with the number of entangled molecules in the solution [45]. Additionally, Table 2 shows that solutions with the same polymer content result in different  $RV$  values for varying  $M_w$ .

Equation (1) and Equation (2) demonstrate that the above-mentioned influence of polymer  $M_w$  on the estimated  $RV$  values derives from the radius of the entangled chain represented by  $R_g$  [56]. In summary, higher  $R_g$  values increase the likelihood of chain collisions and overlapping in solution, leading to the formation of molecular entanglements [45, 56]. Consequently, the increase in molecular interaction for polymers with higher  $M_w$  reduces the onset concentration for the polymeric chains to overlap ( $c^*$ ). Therefore, since  $RV$  grows exponentially with the  $c/c^*$  ratio, as seen in Equation (2), a larger  $c^*$  corresponds to a significantly lower  $RV$  [56]. For example, in 4%  $m/V$  solutions,  $c^*$  ranges from 0.25 to 0.17%  $m/V$  for PHBV  $M_w$  values of  $501 \cdot 10^3$  and  $953 \cdot 10^3 \text{ g} \cdot \text{mol}^{-1}$ ,

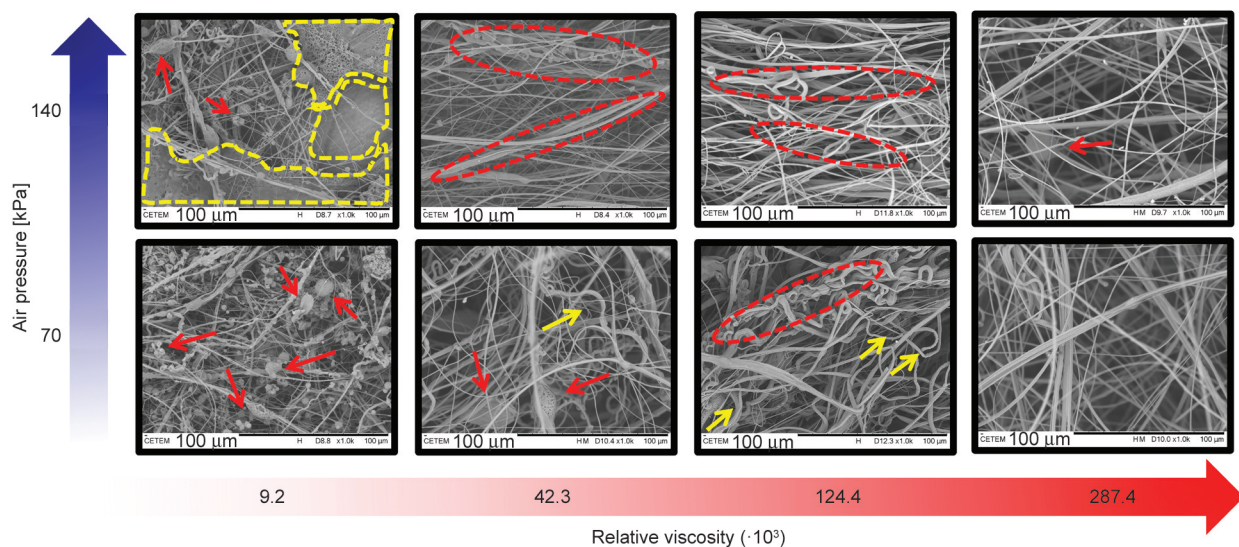
respectively, resulting in corresponding  $RV$  values of  $32.6 \cdot 10^3$  and  $124.5 \cdot 10^3$ . Thus, it is evident that changes in polymer  $M_w$  result in significant variations in solution rheology and should be taken into account in the DoE rather than solely considering the material concentration.

Figure 3 presents the SEM images of the produced PHBV mats spun from solutions with varying viscosities ( $9.2 \cdot 10^3$ ,  $42.3 \cdot 10^3$ ,  $124.4 \cdot 10^3$ , and  $287.4 \cdot 10^3$ ) and at different air pressure –  $AP$  (70 and 140 kPa) to demonstrate the effect of processing parameters on the mats' morphology. At  $RV = 9.2 \cdot 10^3$ , the solution forms fibers with many spherical structures known as beads when spun at 70 kPa. According to Dias *et al.* [49], this type of morphology is characteristic of low-viscous solutions, where the polymeric chain does not form enough entanglements to maintain fiber dimensional stability. As a result, there is sufficient mobility in the chains to form spherical structures with lower surface energy. However, at 140 kPa, cast films form along with the beaded fibers. In these circumstances, the air drag and turbulence of its flow provide instabilities in the still-liquid jet, breaking up the polymeric filament and forming a 'blown spray' deposited as a cast film [45]. For  $RV = 42.3 \cdot 10^3$  at 70 kPa, fibers were formed within a smaller amount of beads. In these conditions, the airflow turbulence effect generates a wave-like bending motion in the polymer jet, which provides filament thinning, aids in solvent evaporation, and deposits bent fibers in the collector [49, 69]. Besides the beads, fiber bundles tend to appear at

140 kPa recurrently from the simultaneous formation of different polymeric jets due to airflow turbulence near the nozzle. PHBV solutions with  $RV = 124.4 \cdot 10^3$  exhibit the same behavior, where a considerable amount of fiber bundles was reported, especially at higher pressures [45, 49].

At  $RV = 287.4 \cdot 10^3$ , the polymeric jet proved stable enough to form beaded-free fibers with controlled morphology when spun at 70 kPa. This finding supports the discussion presented by Dadol *et al.* [48], where increasing viscosity promotes bending-resistant polymeric jets, improving their stability and favoring the formation of non-bent stretched fibers without beads. However, the same solution presented a few beads when spun at 140 kPa concerning the airflow turbulence effect on the polymer jet.

Figure 4 displays a log-log plot of  $RV$  versus the  $c/c^*$  within the semi-dilute regime (where  $c$  represents the solution concentration) based on the results presented in Table 2. According to the estimated values of PHBV solutions  $RV$  and the  $AP$  levels, it is possible to determine the regions of spinnability and the fiber morphology. This determination was based on the morphological analysis discussed above (Figure 3) and the one performed over the fibers spun from the different solutions listed in Table 2 (including the analysis performed by Carlos *et al.* [54]). The results (Figure 4) suggest that a semi-dilute PHBV solution in chloroform can be classified into four different regions according to its spinnability regime. These regions are classified as follows: not spinnable – unentangled (I), spinnable – beaded fibers (II), spinnable



**Figure 3.** Fibers mat's morphology evaluation from PHBV solution with distinct  $RV$  and spun at 70 and 140 kPa. Yellow dotted region – cast film; yellow arrows – bent fibers; red dotted region – fiber bundles; red arrows – beads.

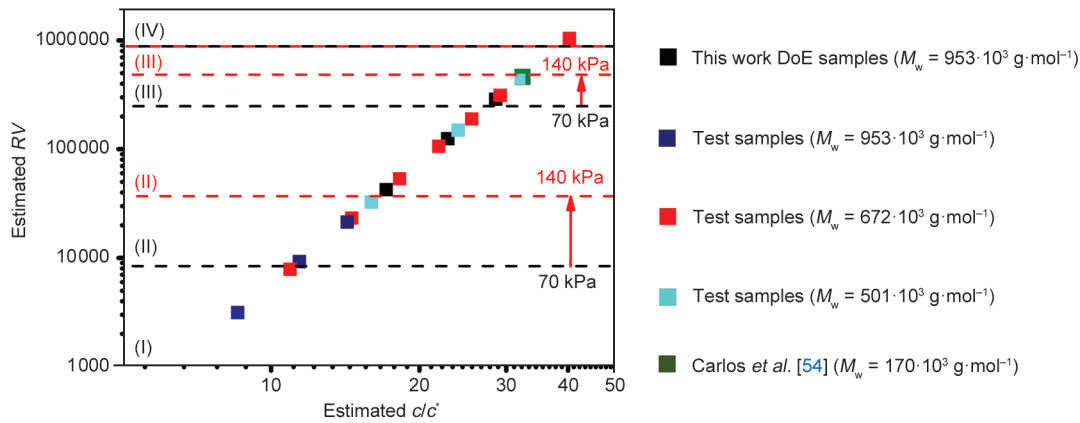


**Figure 4.** Viscometric analysis of the different PHBV solutions over its spinnability regions based on the estimated  $RV$  values as a function of the  $c/c^*$ .

– beads-free fibers (III), and not spinnable – concentrated (IV) [57].

The solution is not spinnable in Region (I), even above  $c^*$  (the onset concentration to the entanglements formation). In this case, the polymeric chains do not sufficiently entangle to sustain the liquid filament shape stability over the air drag stresses in the air/solution interface [48, 54, 57], considering the  $AP$  interval evaluated in this work. Increasing the solution  $RV$  and going to Region (II), the number of entanglements allows the fiber formation, but with spherical structures associated with it, as discussed above [49, 69]. In Region (III), beads-free fibers are formed since the number of entanglements in more viscous solutions restricts the relaxation movements in the polymeric chain that allow the bead's formation [48]. Finally, in Region (IV), the solution enters the concentrated regime, not being spinnable anymore, as the air drag does not overcome the solution's cohesive forces. In this case, the solution droplet ejected from the injection device does not form a polymeric jet. Instead, it evaporates while still in the needle, clogging the nozzle and impeding the spinning process [48, 56].

Besides the previous discussion ascertaining the  $RV$  effect on the spinnability interval, it was also observed in Figure 3 that the morphology of the mat is also affected by the  $AP$  level utilized. For instance, when the solution  $RV$  is around  $9 \cdot 10^3$ , the polymer jet breaks up, forming a spray in 140 kPa [69, 70]. On the other hand, reducing the  $AP$  allows for the formation of fibers with some beads. This occurs because the air drag exerts forces on the liquid polymeric filament, attempting to deform it by stretching the polymeric chains until it breaks. The viscosity of the solution provides resistance to these stretching

movements, affecting the behavior and stability of the jet [48, 54, 57]. In this regard, Figure 4 shows the different limits of the spinnability region for solutions spun at 70 kPa (indicated by black dashed lines) and 140 kPa (indicated by red dashed lines) based on the experimental data obtained.

Figure 4 illustrates that at 70 kPa, solutions are not spinnable for values of  $RV < 10,000$  (Region (I)). Notably, the Region (I) upper limit shifts from  $RV \sim 10,000$  to  $40,000$  for 140 kPa, increasing the minimum amount of entanglements to enable the spinning process. In Region (II), the solution starts being spinnable but with beads due to the chain mobility effect discussed previously. At  $RV \sim 290 \cdot 10^3$ , in the vicinity of Region (III) for solutions spun at 70 kPa fibers without beads were formed [45, 48, 49]. However, the airflow turbulence effect at 140 kPa shifts the upward limit of Region (II) to  $RV \sim 400 \cdot 10^3$ . Finally, for  $RV \sim 10^6$  (in Region (IV)), the resistance to solution deformation in a polymeric jet was too high, which hindered the fiber formation because the solution entered the concentrated regime [48, 49]. Note that the Region (IV) onset  $RV$  values for the solutions spun at 70 and 140 kPa are pretty much close to each other, possibly indicating that this spinnability limit is insensitive for  $AP$  variation (for the levels analyzed in this study), being governed by the viscosity increase in the transition between the semi-dilute to the concentrated regime.

Through the adopted approach for determining the morphology of the fibers, it was also possible to predict the morphology of the fibers produced in the work of Carlos et al. [54]. According to the estimated  $RV$  values based on the solution utilized in their work ( $RV = 460 \cdot 10^3$ ), the morphology should fall within the range of Region (III) for beaded-free



fibers. In fact, the authors found that using a 10%  $m/V$  solution of PHBV ( $M_w = 170 \cdot 10^3 \text{ g} \cdot \text{mol}^{-1}$ ) spun at  $AP = 165, 209, \text{ and } 295 \text{ kPa}$  ( $>140 \text{ kPa}$ ), PHBV fibers with a few defects could be produced, supporting the effect of  $RV$  and  $AP$  on the morphology determination.

### 3.3. Processing parameters effect on the fiber diameter

Figure 5 shows the diameter distribution histograms of each experimental condition evaluated in this work. The histograms embrace all the measurements made in a single fibrous mat, accounting for the different SEM images and totalizing more than 300 measurements. The average values in Figure 5 represent the average diameter of all the fibers analyzed in an experimental condition. The beads were discarded for fiber diameter measurements.

According to Figure 5, higher levels of solution viscosity lead to the formation of thicker fibers with greater diameter dispersion. This can be explained by the fact that a higher quantity of molecular entanglement in more viscous solutions makes it difficult for the polymeric chains to stretch and form thinner fibers [46, 47]. In addition, the formation of a more stable jet at higher viscosities with no bending movement, which would normally cause the polymeric filament to thin, results in larger diameters [66]. For example, nanometric fibers of 590 nm could be obtained at 70 kPa for a PHBV solution

with  $RV = 42.3 \cdot 10^3$ , while micrometric fibers of 1790 nm were obtained with  $RV = 287.4 \cdot 10^3$ . However, to overcome the polymer molecular interactions at higher concentrations, higher airflow shear forces are necessary, allowing the formation of fibers with smaller diameters and low deviation [66]. This effect was observed in fibers spun at 140 kPa, which had a reduced diameter compared to those spun at 70 kPa. For example, PHBV fibers from solutions of  $RV = 42.3 \cdot 10^3$  reduced their diameter by 27%, from 590 nm to 428 nm, when higher air pressure was used.

The results obtained from an ANOVA analysis through the mixed 2-and 3-level design support the earlier discussion. The linear effect of viscosity –  $RV(L)$  was found to be the most significant factor in increasing the average diameter ( $p\text{-value} = 8.5 \cdot 10^{-10}$ ). Additionally, the linear effect of pressure –  $AP(L)$  was statistically significant ( $p\text{-value} = 0.0065$ ), demonstrating the impact of airflow on fiber thinning. However, the linear interaction factor between  $AP$  and  $RV$  ( $I(L)by2(L)$ ) did not significantly affect the fiber diameter ( $p\text{-value} = 0.92$ ), indicating that changes in air pressure from 70 to 140 kPa do not depend on the viscosity levels examined in this study. Furthermore, the quadratic term of viscosity –  $RV(Q)$  ( $p\text{-value} = 0.72$ ) and its interaction factor did not have a significant influence –  $I(Q)by2(L)$  ( $p\text{-value} = 0.66$ ), indicating no quadratic relationship between solution viscosity and diameter.

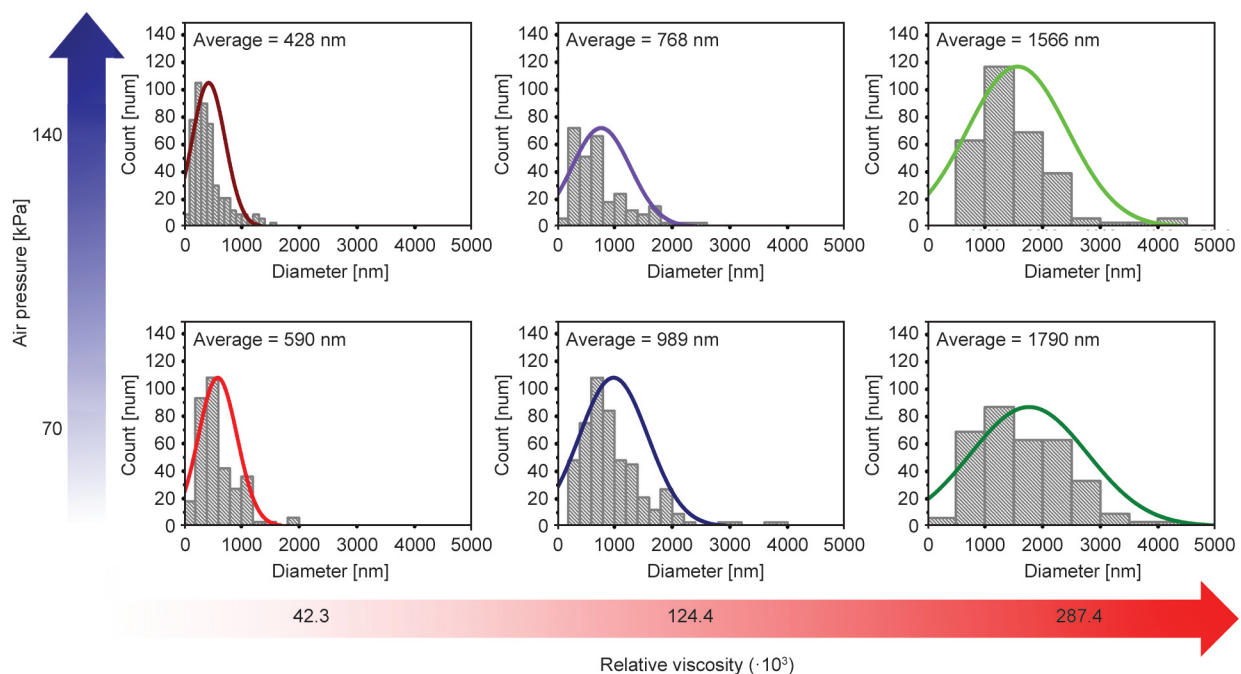


Figure 5. Measured fiber diameters and fiber diameter distribution histograms varying the PHBV solution  $RV$  and  $AP$ .

Based on the regression coefficients calculated through the ANOVA analysis, a strong correlation ( $R^2 = 0.9627 / R_{adj}^2 = 0.9574$ ) was observed between the experimental data for the average diameter and the values predicted by the mathematical model presented in Equation (5). Specifically,  $Y$  denotes the average diameter [nm],  $X_1$  represents the  $RV$ , and  $X_2$  stands for the  $AP$  [kPa]. The model, a reduced version of the one presented in Equation (4), excluded the non-influential factors, such as  $RV(Q)$ ,  $I(L)by2(L)$ , and  $I(Q)by2(L)$ . Therefore, the regression coefficients  $\beta_3$ ,  $\beta_4$ , and  $\beta_5$ , (shown in Equation (4)) correlated to each of those non-influential factors that were considered null. Additionally, the model indicates normality in the error term, and the variation

of the predicted values from the experimental consequences implies no systematic bias [46, 71]. As a result, Figure 6a displays the surface response plot generated based on the developed model for diameter prediction (Equation (5)):

$$Y = 575.11 - 2.59 \cdot X_2 + 0.004 \cdot X_1 \quad (5)$$

Figure 6b depicts the trend of predicted values versus experimental values, where the majority of experimental points overlap with the line of predicted values, affirming the accuracy of the model (Equation (5)). Therefore, to evaluate the model's predictive capability for the average diameter of PHBV fibers, Table 3 presents test samples produced from different

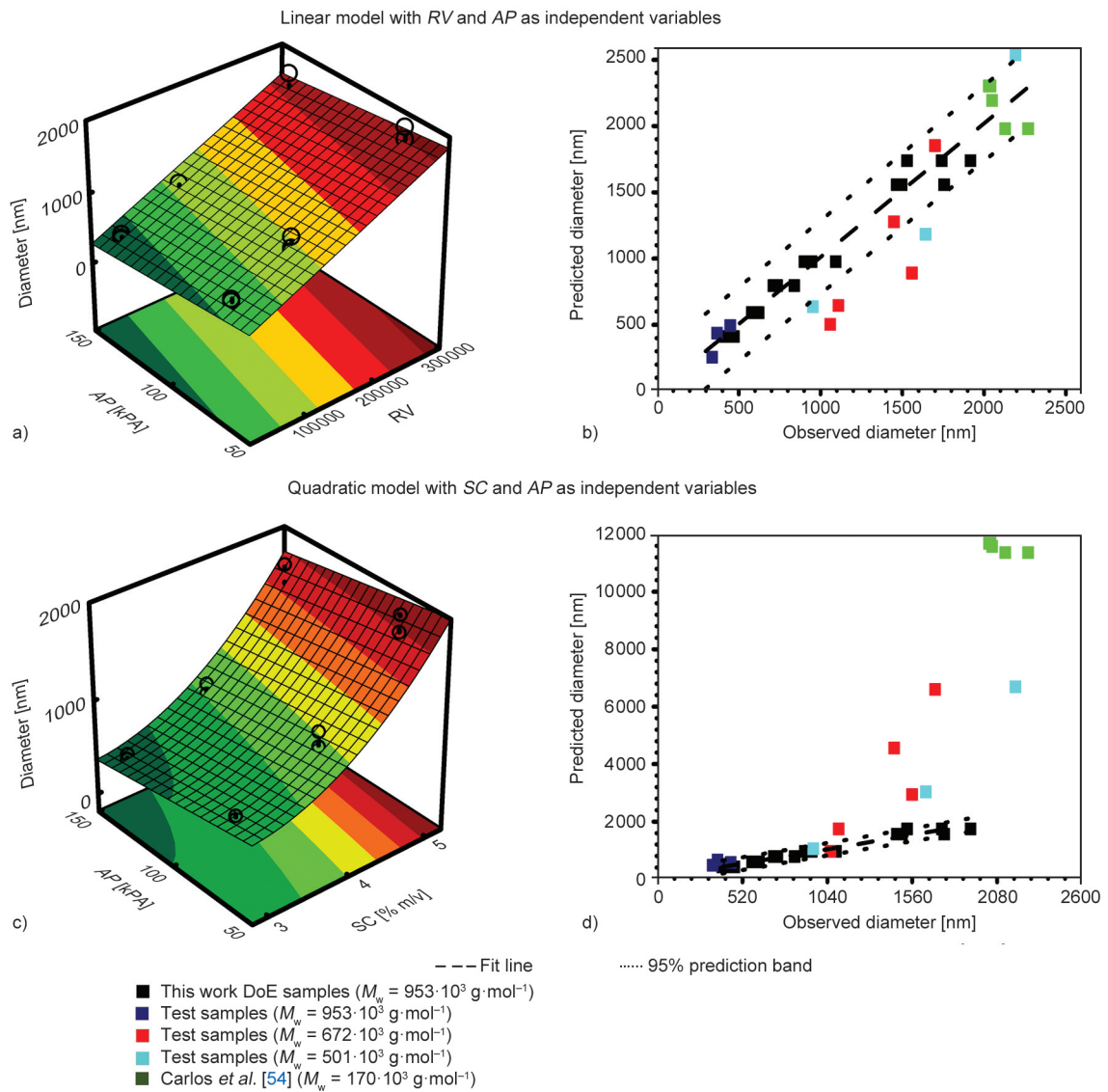


**Figure 6.** Comparison between the ANOVA models for PHBV fiber diameter prediction: a) response surface plot of diameter and b) predicted fiber diameters against experimental values from the DoE using  $RV$  and  $AP$  as independent variables; c) response surface plot of diameter and d) predicted fiber diameters against experimental values from the DoE using  $SC$  and  $AP$  as independent variables.

**Table 3.** Average diameter predicted values [nm].

<i>SC</i> [% <i>m/V</i> ]	<i>RV</i> [10 <sup>3</sup> ]	<i>AP</i> [kPa]	Predicted diameter values <sup>a</sup> [nm]	Predicted diameter values <sup>b</sup> [nm]
<b>This work DoE samples (<math>M_w = 953 \cdot 10^3 \text{ g} \cdot \text{mol}^{-1}</math>)</b>				
3	42.3	70	592	601
3	42.3	140	411	420
4	124.4	70	976	962
4	124.4	140	795	781
5	287.4	70	1737	1742
5	287.4	140	1556	1561
<b>Test samples (<math>M_w = 953 \cdot 10^3 \text{ g} \cdot \text{mol}^{-1}</math>)</b>				
2	9.2	70	437	659
2.5	21.3	70	494	578
<b>Test samples (<math>M_w = 672 \cdot 10^3 \text{ g} \cdot \text{mol}^{-1}</math>)</b>				
4	23.1	70	502	962
5	53.5	70	644	1742
6	106.0	70	890	2942
7	189.0	70	1277	4560
8	311.8	70	1851	6598
<b>Test samples (<math>M_w = 501 \cdot 10^3 \text{ g} \cdot \text{mol}^{-1}</math>)</b>				
4	32.6	35	637	1053
6	149.3	35	1183	3032
8	439.3	35	2537	6688
<b>Carlos et al. [54] (<math>M_w = 170 \cdot 10^3 \text{ g} \cdot \text{mol}^{-1}</math>)</b>				
10	460.8	165	2302	11 685
10	460.8	207	2193	11 576
10	460.8	290	1978	11 361

<sup>a</sup>Predicted values based on the ANOVA model using the *RV*;

<sup>b</sup>Predicted values based on the ANOVA model using *SC*.

$M_w$  with varying *RV* and *AP* values. Almost all experimental average diameters of the samples align with those predicted by the model within their respective predictive intervals (95% prediction band). Additionally, the model was also successful in predicting the fiber diameter from Carlos *et al.* [54] work.

A quadratic model was generated using PHBV solution concentration (*SC*) instead of *RV*, considering only the significant factor that provided the highest  $R_{\text{adj}}^2$  value (0.9548) based on the DoE to compare their effectiveness as independent variables in predicting the fibers' average diameter. The response surface plot in Figure 6c evidences the quadratic dependence of the average diameter with *SC* in the generated model. However, most of the test samples with varying  $M_w$ , including those from Carlos *et al.* [54] study, lie far outside the 95% prediction band, as shown in Figure 6d, which compares the predicted with the experimental values. These results suggest that concentration may not be the most suitable variable in a DoE for predicting SBS-fiber diameter, as it does not account for the impact of polymer  $M_w$  variations.

### 3.4. Processing parameters effect on the fiber orientation

In addition to changes in diameter, the *AP* and *RV* are responsible for the fiber's orientation. The air in contact with the solid and static collector spreads in the radial direction, promoting the fibers to align towards the direction of their scattering [10]. The degree or amount of this alignment depends on the resistance that the polymer jet promotes to deform in the airflow direction. In other words, the stability of the jet is also responsible for reducing the degree of the alignment of the fibers deposited in the collector [45, 66].

Having said that, in order to evaluate the influence of the processing variables on the fiber alignment, the SEM images were subjected to orientation distribution and alignment analysis using the OrientationJ plugin from ImageJ software [54, 59, 60]. The results shown in Figure 7a were obtained through orientation distribution curves, varying the fibers' orientation angles from  $-90^\circ$  to  $90^\circ$ , while Figure 7b presents the calculated alignment index (*AI*) values.

Color maps were produced to visualize the orientation distribution of the fibers in the mats [60]. In fibers produced from solution with  $RV = 42.3 \cdot 10^3$  and  $124.4 \cdot 10^3$ , the deposition angle was shown to be influenced by the effect of  $AP$ . At 70 kPa, such fibers did not show a preferential orientation, with a dispersed orientation distribution and average  $AI$  values of 60 and 63, respectively, indicating the formation of more random fibers. However, at 140 kPa, the mentioned fibers showed a preferential alignment, as can be seen in the orientation peaks close to  $0^\circ$  and new  $AI$  of 71 and 66%, respectively. On the other hand, for  $RV = 287.4 \cdot 10^3$  the effect of polymeric entanglements promoted resistance to alignment despite the air pressure value. When spun at 70 kPa, the fibers were deposited more randomly, while at 140 kPa, there was no formation of a single

orientation peak, but a more distributed curve with up to 3 peaks between  $-50^\circ$  and  $50^\circ$ . The ANOVA results based on the  $AI$  response values indicated that the drag force generated by the  $AP(L)$  is the most significant factor for the alignment of the fiber ( $p$ -value = 0.0003), followed by the  $RV(L)$  ( $p$ -value = 0.0027), corroborating with the previous discussion. In addition, the  $I(L)by2(L)$  was also influential ( $p$ -value = 0.0063), endorsing that the polymeric jet stability in more viscous solutions decreases the air drag alignment at higher  $AP$  levels. Finally, the  $RV(Q)$  also proved marginally influential ( $p$ -value = 0.0233). Thus, this work presents the possibility of obtaining PHBV fibers oriented in the radial direction using a solid and static collector, controlling the degree of this orientation through air pressure and PHBV concentration.

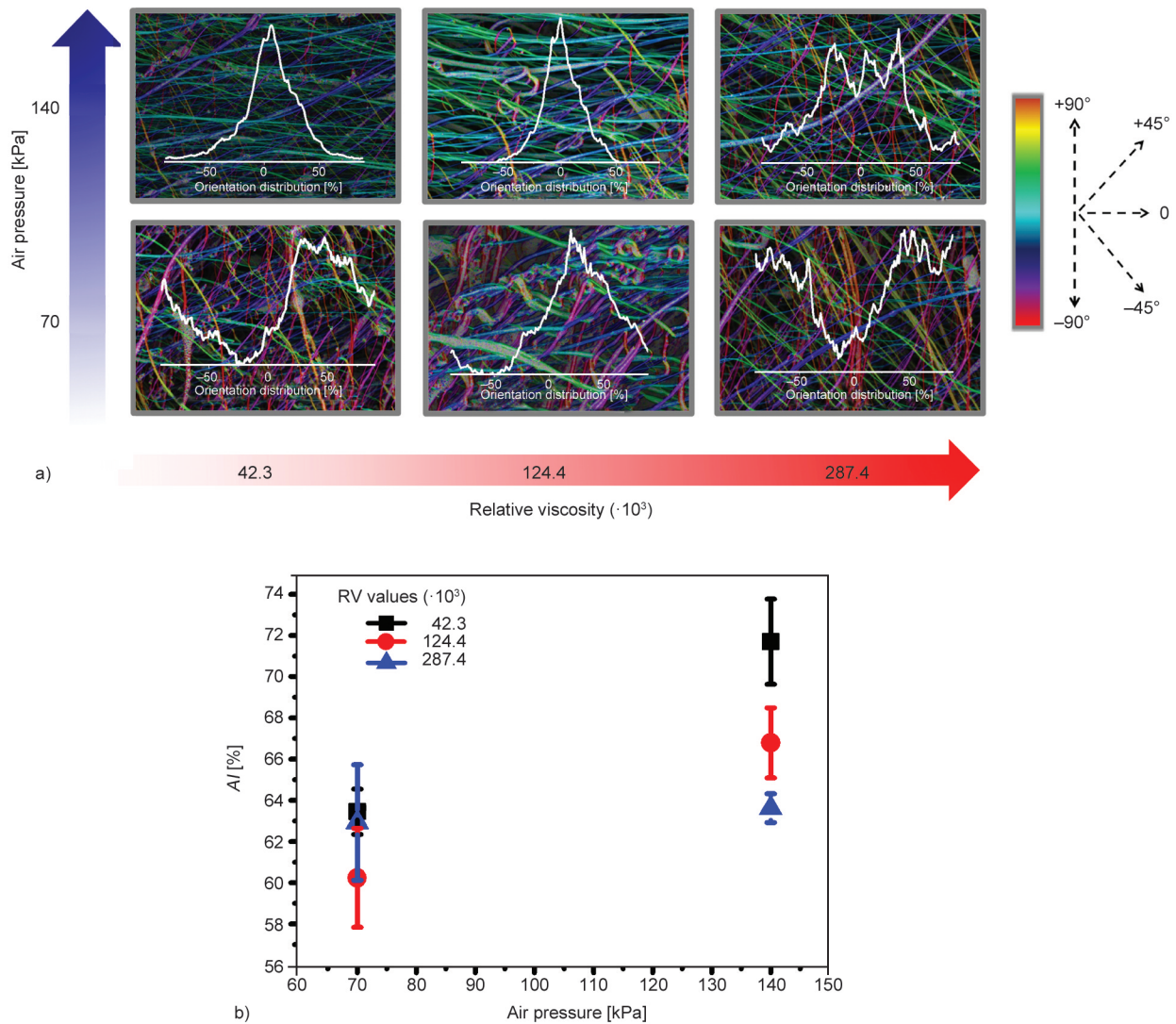
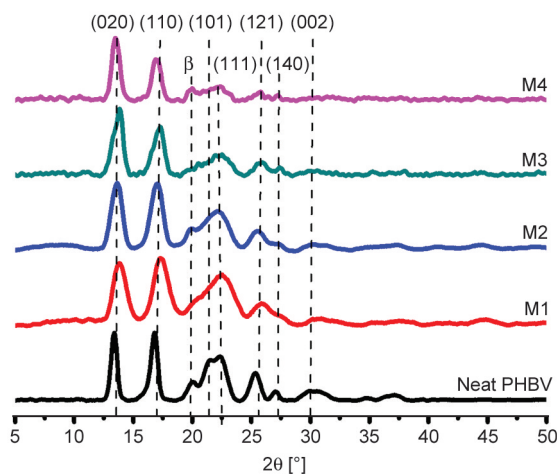


Figure 7. Fiber orientation analysis: a) mat's orientation distribution curves, and b) fibers  $AI$  response values.

### 3.5. Mats' crystalline analysis

Figure 8 presents the normalized X-ray diffractograms of the produced mats and the neat PHBV powder. Characteristic peaks of PHBV are observed for all samples at  $2\theta$  around  $14^\circ$ ,  $17^\circ$ ,  $22^\circ$ ,  $23^\circ$ ,  $26^\circ$ ,  $27^\circ$ , and  $30^\circ$ , which correspond to the planes (020), (110), (101), (111), (121), (040), and (002), respectively. These peaks refer to the helix conformation of the PHBV chains organized in an orthorhombic crystal lattice ( $\alpha$ -form) [72]. For the samples spun at 140 kPa and the neat PHBV, it was possible to observe a crystalline peak at  $20.5^\circ$ , referring to the  $\beta$ -form of the planar zig-zag conformation. According to Mottin *et al.* [73], the  $\beta$ -form depends on greater forces that induce the stretching and alignment of the polymeric chains to trap them in the planar zig-zag conformation. In addition, the  $\beta$ -form is correlated with the fibers' alignment [73], corroborating with the results observed for the AI (Figure 7). Therefore, the spinning pressure of 140 kPa favored the formation of the  $\beta$ -form in the PHBV mats crystalline lattice, which disappeared for the 70 kPa-spun samples compared to the neat material.

The effect of the spinning process parameter variations on the shape of the diffractograms' peaks that correspond to the (020) and (110) planes was evaluated using the interplanar spacing ( $d$ ) and crystallite size ( $D$ ). Figure 9a contains the measured values for  $d$  of the orthorhombic structures corresponding to the (020) and (110) planes. As can be seen, both  $d_{020}$



**Figure 8.** Mats' and neat PHBV's normalized X-ray diffractograms. M1 – mats spun at 70 kPa from solutions with  $RV = 42.3 \cdot 10^3$ ; M2 – mats spun at 140 kPa from solutions with  $RV = 42.3 \cdot 10^3$ ; M3 – mats spun at 70 kPa from solutions with  $RV = 287.4 \cdot 10^3$ ; and M4 – mats spun at 140 kPa from solutions with  $RV = 287.4 \cdot 10^3$ .

and  $d_{110}$  did not show significant variation after the spinning process compared to the neat material ( $p$ -value  $> 0.05$ ). They also remained insensitive to changes in processing parameters such as  $AP$  and  $RV$ , indicating a non-significant variation in the positioning of the crystalline peaks. Similar results were observed in the study by Souza *et al.* [55], where the type of processing undergone by PHBV did not alter the  $d$ -spacing for the same analyzed planes.

Figure 9b presents the values of  $D$  for the peaks corresponding to the (020) and (110) planes.  $D$  was significantly reduced after the spinning process compared to the neat material ( $p$ -value  $< 0.05$ ) associated with the rapid evaporation of the material during the solution blow spinning process and corroborated by the peaks broadening [55]. Similarly,  $D_{110}$  and  $D_{020}$  were affected by the levels of  $AP$  applied. Higher spinning pressures resulted in smaller crystalline structures for both (020) and (110) planes. However, an increase in viscosity led to the formation of larger crystals, narrowing the crystalline peaks. In the case of the mats produced under the M3 condition, a shoulder could be perceived in both analyzed planes (Figure 9c), indicating two different crystallite sizes. Therefore, two measurements were performed for this condition, as shown in Figures 9a and 9b as M3(1) and M3(2). The  $d$ -spacing and the crystal size followed the above-described trends for both cases.

Figure 9d shows the calculated values for the mats and neat PHBV crystallinity index [%] from the integrated area below the crystalline peaks. Notably, the SBS process is responsible for reducing the fibers' crystallinity since the neat polymer obtained a  $CI$  [%] equal to 77.4, higher than those from the produced mats ( $p$ -value  $< 0.05$ ). This effect is consistent with the literature since the fibers undergo rapid solidification during their trajectory to the collector in the SBS process, as exemplified in Figure 9e. Consequently, the degree of organization of the crystalline phase chains is reduced compared to the neat material [55].

ANOVA results for the  $CI$  [%] response indicate that the spinning conditions are significant for the spun material crystallinity.  $CI$  [%] is reduced with increasing  $RV(L)$  ( $p$ -value =  $2.4 \cdot 10^{-7}$ ) due to the restriction to chain movement into an organized crystalline lattice by the effect of the entanglements during solidification. Higher  $AP(L)$  levels were responsible for the increase in  $CI$  ( $p$ -value = 0.0017), probably related to the formation of  $\beta$ -form. The  $I(L)by2(L)$  factor

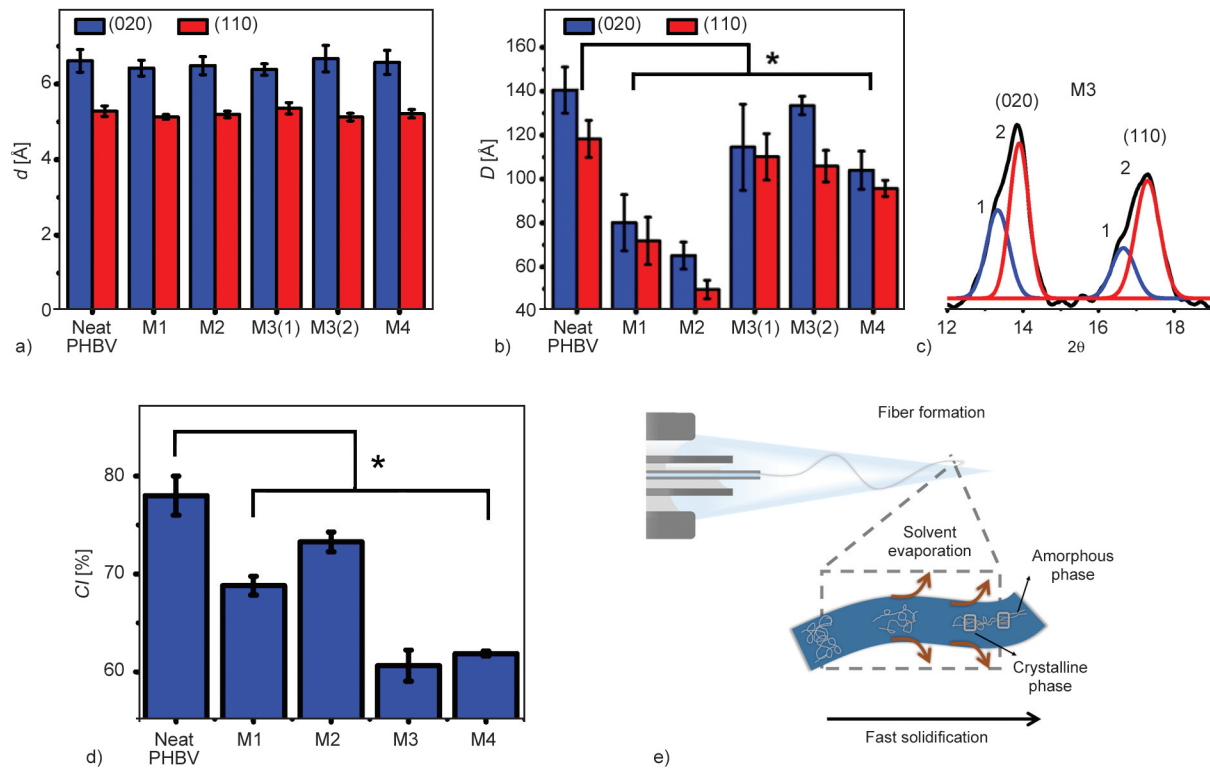


**Figure 9.** Mats' and neat PHBV's crystalline analysis: a) interplanar spacing [ $\text{\AA}$ ], b) crystallite size [ $\text{\AA}$ ], c) M3 mat's crystalline peaks deconvolution, d) crystallinity index values [%], and e) fibers solidification scheme. M1 – mats spun at 70 kPa from solutions with  $RV = 42.3 \cdot 10^3$ ; M2 – mats spun at 140 kPa from solutions with  $RV = 42.3 \cdot 10^3$ ; M3 – mats spun at 70 kPa from solutions with  $RV = 287.4 \cdot 10^3$ ; and M4 – mats spun at 140 kPa from solutions with  $RV = 287.4 \cdot 10^3$ . \* $p$ -value < 0.05.

proved marginally significant ( $p$ -value = 0.030), suggesting that the less-viscous ( $RV = 42.3 \cdot 10^3$ ) solutions are more susceptible to crystallization during the fiber formation at higher pressures than more viscous solutions ( $RV = 287.4 \cdot 10^3$ ). Finally, these results suggest that above some limit air velocity, which still must be studied, the PHBV amorphous phase tends to get re-oriented induced by air drag forces, increasing the  $CI$  [%], even though the fast solidification process significantly decreases the material crystallinity.

#### 4. Conclusion

PHBV fibrous mats were produced via SBS and had their diameter, morphology, orientation, and crystallinity evaluated through a systematic study of the processing variables. In this study, we proposed the utilization of the theoretical  $RV$  as an independent variable instead of the solution concentration to account for the polymer's  $M_w$  variation effect on the mat's properties. The ANOVA results showed that the increase in the  $RV$  favored the formation of thicker fibers ( $p$ -value =  $8.5 \cdot 10^{-10}$ ) with lower  $AI$

( $p$ -value = 0.002) and  $CI$  [%] ( $p$ -value =  $2.4 \cdot 10^{-7}$ ) values. Higher  $AP$  levels contributed to thinner ( $p$ -value = 0.0061) and more aligned fibers ( $p$ -value = 0.0001). The chain's stretching driven by air drag at 140 kPa increased the crystallinity ( $p$ -value = 0.0017) due to PHBV  $\beta$ -phase formation. Schlieren's visualization method was innovatively utilized for an SBS system with co-axial needles to visualize the airflow profile as it leaves the injection device at different pressures. It was possible to infer by the low- and high-density zones seen by Schlieren's method that the airflow at 70 kPa was more laminar when compared to 140 kPa, turbulent. The latter induced the formation of fiber bundles and beads. Based on the estimated  $RV$  and  $AP$  levels, it was also possible to identify the regions where spinning is feasible and determine the morphology of the fibers produced. Defect-free fibers could be obtained in  $RV = 290 \cdot 10^3$ – $10^6$  at 70 kPa, while for 140 kPa, between  $400 \cdot 10^3$  and  $10^6$ . The developed ANOVA model demonstrated good predictive capacity ( $R_{adj}^2 = 0.96$ ) over the average diameter of PHBV fibers produced by the SBS technique, even when

polymers with distinct  $M_w$  values were utilized. Overall, fibers with diameters varying from 428 to 989 nm were produced from PHBV solutions with  $RV = 42.3 \cdot 10^3$ – $124.4 \cdot 10^3$ , while microfibers (1.56–1.99  $\mu\text{m}$ ) from solutions  $RV = 287.4 \cdot 10^3$ . Finally, the morphology and diameter determination presented in this work via the theoretical  $RV$  estimate, aligned with a low-cost processing technique like SBS, make PHBV an attractive biodegradable material for several applications, especially those where the reproducibility in the microstructural properties directly affects its efficiency.

### Acknowledgements

The authors kindly acknowledge the Brazilian agencies Coordination of Superior Level Staff (CAPES), Fundação Carlos Chagas Filho de Amparo à Pesquisa do Estado do Rio de Janeiro (FAPERJ) and National Council for Scientific and Technological Development (CNPq) for the financial support, to the Multi-user Laboratory of Materials Characterization of the Program of Metallurgical and Materials Engineering (PEMM)/COPPE/UFRJ for XRD analysis, to the Thermal Analysis and Rheology Laboratory, located in the Center for Biofuels, Petroleum and its Derivatives (EQ/UFRJ) for the rheological experiment's assistance, and to CETEM for the SEM analysis.

### References

- [1] Li X., Zhuang Z., Qi D., Zhao C.: High sensitive and fast response humidity sensor based on polymer composite nanofibers for breath monitoring and non-contact sensing. *Sensors and Actuators B: Chemical*, **330**, 129239 (2021).  
<https://doi.org/10.1016/j.snb.2020.129239>
- [2] Wang S., Shi K., Chai B., Qiao S., Huang Z., Jiang P., Huang X.: Core-shell structured silk fibroin/PVDF piezoelectric nanofibers for energy harvesting and self-powered sensing. *Nano Materials Science*, **4**, 126–132 (2022).  
<https://doi.org/10.1016/j.nanoms.2021.07.008>
- [3] Abolhasani M. M., Azimi S., Mousavi M., Anwar S., Hassanpour Amiri M., Shirvanimoghaddam K., Naebe M., Michels J., Asadi K.: Porous graphene/poly(vinylidene fluoride) nanofibers for pressure sensing. *Journal of Applied Polymer Science*, **139**, 51907 (2022).  
<https://doi.org/10.1002/app.51907>
- [4] Souzandeh H., Wang Y., Netravali A. N., Zhong W-H.: Towards sustainable and multifunctional air-filters: A review on biopolymer-based filtration materials. *Polymer Reviews*, **59**, 651–686. (2019).  
<https://doi.org/10.1080/15583724.2019.1599391>
- [5] Xu J., Xiao X., Zhang W., Xu R., Kim S. C., Cui Y., Howard T. T., Wu E., Cui Y.: Air-filtering masks for respiratory protection from PM<sub>2.5</sub> and pandemic pathogens. *One Earth*, **3**, 574–589 (2020).  
<https://doi.org/10.1016/j.oneear.2020.10.014>
- [6] Lv D., Zhu M., Jiang Z., Jiang S., Zhang Q., Xiong R., Huang C.: Green electrospun nanofibers and their application in air filtration. *Macromolecular Materials and Engineering*, **303**, 1800336 (2018).  
<https://doi.org/10.1002/mame.201800336>
- [7] Tan N. P. B., Paclijan S. S., Ali H. N. M., Hallazgo C. M. J. S., Lopez C. J. F., Eborá Y. C.: Solution blow spinning (SBS) nanofibers for composite air filter masks. *ACS Applied Nano Materials*, **2**, 2475–2483 (2019).  
<https://doi.org/10.1021/acsanm.9b00207>
- [8] Makaremi M., De Silva R. T., Pasbakhsh P.: Electrospun nanofibrous membranes of polyacrylonitrile/halloysite with superior water filtration ability. *The Journal of Physical Chemistry C*, **119**, 7949–7958 (2015).  
<https://doi.org/10.1021/acs.jpcc.5b00662>
- [9] Park J. C., Kim J-C., Park S., Kim D-W.: Efficient waste polyvinyl(butylal) and cellulose composite enabled carbon nanofibers for oxygen reduction reaction and water remediation. *Applied Surface Science*, **510**, 145505 (2020).  
<https://doi.org/10.1016/j.apsusc.2020.145505>
- [10] Sow P. K., Ishita, Singhal R.: Sustainable approach to recycle waste polystyrene to high-value submicron fibers using solution blow spinning and application towards oil-water separation. *Journal of Environmental Chemical Engineering*, **8**, 102786 (2020).  
<https://doi.org/10.1016/j.jece.2018.11.031>
- [11] Hiremath N., Evora M. C., Naskar A. K., Mays J., Bhat G.: Polyacrylonitrile nanocomposite fibers from acrylonitrile-grafted carbon nanofibers. *Composites Part B: Engineering*, **130**, 64–69 (2017).  
<https://doi.org/10.1016/j.compositesb.2017.07.031>
- [12] Zheng N., Liu H-Y., Gao J., Mai Y-W.: Synergetic improvement of interlaminar fracture energy in carbon fiber/epoxy composites with nylon nanofiber/polycaprolactone blend interleaves. *Composites Part B: Engineering*, **171**, 320–328 (2019).  
<https://doi.org/10.1016/j.compositesb.2019.05.004>
- [13] Pham L. Q., Uspenskaya M. V., Olekhovich R. O., Bernal R. A. O.: A review on electrospun PVC nanofibers: Fabrication, properties, and application. *Fibers*, **9**, 12 (2021).  
<https://doi.org/10.3390/fib9020012>
- [14] Karagoz S., Kiremitler N. B., Sarp G., Pekdemir S., Salem S., Goksu A. G., Onses M. S., Sozdutmaz I., Sahmetlioglu E., Ozkara E. S., Ceylan A., Yilmaz E.: Antibacterial, antiviral, and self-cleaning mats with sensing capabilities based on electrospun nanofibers decorated with ZnO nanorods and Ag nanoparticles for protective clothing applications. *ACS Applied Materials and Interfaces*, **13**, 5678–5690 (2021).  
<https://doi.org/10.1021/acsami.0c15606>

- [15] Chiu C-W., Huang C-Y., Li J-W., Li C-L.: Flexible hybrid electronics nanofiber electrodes with excellent stretchability and highly stable electrical conductivity for smart clothing. *ACS Applied Materials and Interfaces*, **14**, 42441–42453 (2022).  
<https://doi.org/10.1021/acsami.2c11724>
- [16] Kaniuk Ł., Stachewicz U.: Development and advantages of biodegradable PHA polymers based on electrospun PHBV fibers for tissue engineering and other biomedical applications. *ACS Biomaterials Science and Engineering*, **7**, 5339–5362 (2021).  
<https://doi.org/10.1021/acsbiomaterials.1c00757>
- [17] Dalgic A. D., Koman E., Karatas A., Tezcaner A., Keskin D.: Natural origin bilayer pullulan-PHBV scaffold for wound healing applications. *Biomaterials Advances*, **134**, 112554 (2022).  
<https://doi.org/10.1016/j.msec.2021.112554>
- [18] Paschoalin R. T., Traldi B., Aydin G., Oliveira J. E., Rütten S., Mattoso L. H., Zenke M., Sechi A.: Solution blow spinning fibres: New immunologically inert substrates for the analysis of cell adhesion and motility. *Acta Biomaterialia*, **51**, 161–174 (2017).  
<https://doi.org/10.1016/j.actbio.2017.01.020>
- [19] Rivera-Briso A. L., Serrano-Aroca A.: Poly(3-hydroxybutyrate-co-3-hydroxyvalerate): Enhancement strategies for advanced applications. *Polymers*, **10**, 732 (2018).  
<https://doi.org/10.3390/polym10070732>
- [20] Simbara M. M., Santos Jr A. R., Andrade A. J., Malmonge S. M.: Comparative study of aligned and non-aligned poly( $\epsilon$ -caprolactone) fibrous scaffolds prepared by solution blow spinning. *Journal of Biomedical Materials Research Part B: Applied Biomaterials*, **107**, 1462–1470 (2019).  
<https://doi.org/10.1002/jbm.b.34238>
- [21] Magaz A., Roberts A. D., Faraji S., Nascimento T. R., Medeiros E. S., Zhang W., Greenhalgh R. D., Mautner A., Li X., Blaker J. J.: Porous, aligned, and biomimetic fibers of regenerated silk fibroin produced by solution blow spinning. *Biomacromolecules*, **19**, 4542–4553 (2018).  
<https://doi.org/10.1021/acs.biomac.8b01233>
- [22] Tomecka E., Wojasinski M., Jastrzebska E., Chudy M., Ciach T., Brzozka Z.: Poly(L-lactic acid) and polyurethane nanofibers fabricated by solution blow spinning as potential substrates for cardiac cell culture. *Materials Science and Engineering: C*, **75**, 305–316 (2017).  
<https://doi.org/10.1016/j.msec.2017.02.055>
- [23] Kaniuk Ł., Ferraris S., Spriano S., Luxbacher T., Krysiak Z., Berniak K., Zaszczynska A., Marzec M. M., Bernasik A., Sajkiewicz P., Zaszczynska A., Marzec M. M., Bernasik A., Stachewicz U.: Time-dependent effects on physicochemical and surface properties of PHBV fibers and films in relation to their interactions with fibroblasts. *Applied Surface Science*, **545**, 148983 (2021).  
<https://doi.org/10.1016/j.apsusc.2021.148983>
- [24] dos Santos D. M., Correa D. S., Medeiros E. S., Oliveira J. E., Mattoso L. H.: Advances in functional polymer nanofibers: From spinning fabrication techniques to recent biomedical applications. *ACS Applied Materials and Interfaces*, **12**, 45673–45701 (2020).  
<https://doi.org/10.1021/acsami.0c12410>
- [25] Medeiros E. L. G., Braz A. L., Porto I. J., Menner A., Bismarck A., Boccaccini A. R., Lepry W. C., Nazhat S. N., Medeiros E. S., Blaker J. J.: Porous bioactive nanofibers *via* cryogenic solution blow spinning and their formation into 3D macroporous scaffolds. *ACS Biomaterials Science and Engineering*, **2**, 1442–1449 (2016).  
<https://doi.org/10.1021/acsbiomaterials.6b00072>
- [26] Kuppan P., Vasanthan K. S., Sundaramurthi D., Krishnan U. M., Sethuraman S.: Development of poly(3-hydroxybutyrate-co-3-hydroxyvalerate) fibers for skin tissue engineering: Effects of topography, mechanical, and chemical stimuli. *Biomacromolecules*, **12**, 3156–3165 (2011).  
<https://doi.org/10.1021/bm200618w>
- [27] Yilmaz S. S., Aytac A.: Fabrication and characterization as antibacterial effective wound dressing of hollow polylactic acid/polyurethane/silver nanoparticle nanofiber. *Journal of Polymer Research*, **29**, 473 (2022).  
<https://doi.org/10.1007/s10965-022-03309-7>
- [28] Singh S., Mohanty A. K., Sugie T., Takai Y., Hamada H.: Renewable resource based biocomposites from natural fiber and polyhydroxybutyrate-co-valerate (PHBV) bioplastic. *Composites Part A: Applied Science and Manufacturing*, **39**, 875–886 (2008).  
<https://doi.org/10.1016/j.compositesa.2008.01.004>
- [29] Pal A. K., Wu F., Misra M., Mohanty A. K.: Reactive extrusion of sustainable PHBV/PBAT-based nanocomposite films with organically modified nanoclay for packaging applications: Compression moulding vs. cast film extrusion. *Composites Part B: Engineering*, **198**, 108141 (2020).  
<https://doi.org/10.1016/j.compositesb.2020.108141>
- [30] Lajewski S., Mauch A., Geiger K., Bonten C.: Rheological characterization and modeling of thermally unstable poly(3-hydroxybutyrate-co-3-hydroxyvalerate) (PHBV). *Polymers*, **13**, 2294 (2021).  
<https://doi.org/10.3390/polym13142294>
- [31] Policastro G., Panico A., Fabbicino M.: Improving biological production of poly(3-hydroxybutyrate-co-3-hydroxyvalerate) (PHBV) *co*-polymer: A critical review. *Reviews in Environmental Science and Bio/Technology*, **20**, 479–513 (2021).  
<https://doi.org/10.1007/s11157-021-09575-z>
- [32] Gironi F., Piemonte V.: Bioplastics and petroleum-based plastics: Strengths and weaknesses. *Energy Sources Part A: Recovery, Utilization, and Environmental Effects*, **33**, 1949–1959 (2011).  
<https://doi.org/10.1080/15567030903436830>



- [33] Rabbani S., Jafari R., Momen G.: Superhydrophobic micro-nanofibers from PHBV-SiO<sub>2</sub> biopolymer composites produced by electrospinning. *Functional Composite Materials*, **3**, 1 (2022).  
<https://doi.org/10.1186/s42252-022-00029-5>
- [34] Liu Y., Chen X., Yu D-G., Liu H., Liu Y., Liu P.: Electrospun PVP-core/PHBV-shell fibers to eliminate tailing off for an improved sustained release of curcumin. *Molecular Pharmaceutics*, **18**, 4170–4178 (2021).  
<https://doi.org/10.1021/acsmolpharmaceut.1c00559>
- [35] Carli L. N., Bianchi O., Machado G., Crespo J. S., Mauler R. S.: Morphological and structural characterization of PHBV/organoclay nanocomposites by small angle X-ray scattering. *Materials Science and Engineering: C*, **33**, 932–937 (2013).  
<https://doi.org/10.1016/j.msec.2012.11.023>
- [36] Karbowniczek J. E., Kaniuk L., Berniak K., Gruszczynski A., Stachewicz U.: Enhanced cells anchoring to electrospun hybrid scaffolds with PHBV and HA particles for bone tissue regeneration. *Frontiers in Bioengineering and Biotechnology*, **9**, 632029 (2021).  
<https://doi.org/10.3389/fbioe.2021.632029>
- [37] de Carvalho Benini K. C. C., Ornaghi H. L., de Medeiros N. M., Pereira P. H. F., Cioffi M. O. H.: Thermal characterization and lifetime prediction of the PHBV/nanocellulose biocomposites using different kinetic approaches. *Cellulose*, **27**, 7503–7522 (2020).  
<https://doi.org/10.1007/s10570-020-03318-z>
- [38] Hammiche D., Boukerrou A., Grohens Y., Guermazi N., Arrakhiz F. E.: Mechanical properties and biodegradation of biocomposites based on poly(hydroxybutyrate-co-valerate) and alfa fibers. *Journal of Polymer Research*, **27**, 308 (2020).  
<https://doi.org/10.1007/s10965-020-02284-1>
- [39] Peshne H., Satapathy B. K.: Comparative studies of structural, thermal, mechanical, rheological and dynamic mechanical response of melt mixed PHB/bio-PBS and PHBV/bio-PBS blends. *Journal of Polymer Research*, **29**, 496 (2022).  
<https://doi.org/10.1007/s10965-022-03323-9>
- [40] Kanda G. S., Al-Qaradawi I., Luyt A. S.: Morphology and property changes in PLA/PHBV blends as function of blend composition. *Journal of Polymer Research*, **25**, 196 (2018).  
<https://doi.org/10.1007/s10965-018-1586-3>
- [41] Kaniuk L., Podborska A., Stachewicz U.: Enhanced mechanical performance and wettability of PHBV fiber blends with evening primrose oil for skin patches improving hydration and comfort. *Journal of Materials Chemistry B*, **10**, 1763–1774 (2022).  
<https://doi.org/10.1039/d1tb02805g>
- [42] Alane A., Zembouai I., Benhamida A., Zaidi L., Touati N., Kaci M.: Opuntia ficus indica fibers as reinforcement in PHBV biocomposites. *Materials Today: Proceedings*, **53**, 218–222 (2022).  
<https://doi.org/10.1016/j.matpr.2022.01.030>
- [43] Upson S. J., O’Haire T., Russell S. J., Dalgarno K., Ferreira A. M.: Centrifugally spun PHBV micro and nanofibres. *Material Science and Engineering C*, **76**, 190–195 (2017).  
<https://doi.org/10.1016/j.msec.2017.03.101>
- [44] Erben J., Kalous T., Chvojka J.: AC bubble electrospinning technology for preparation of nanofibrous mats. *ACS Omega*, **5**, 8268–8271 (2020).  
<https://doi.org/10.1021/acsomega.0c00575>
- [45] Daristotle J. L., Behrens A. M., Sandler A. D., Kofinas P.: A review of the fundamental principles and applications of solution blow spinning. *ACS Applied Materials and Interfaces*, **8**, 34951–34963 (2016).  
<https://doi.org/10.1021/acsmi.6b12994>
- [46] da Silva Parize D. D., Foschini M. M., de Oliveira J. E., Klamczynski A. P., Glenn G. M., Marconcini J. M., Mattoso L. H. C.: Solution blow spinning: Parameters optimization and effects on the properties of nanofibers from poly(lactic acid)/dimethyl carbonate solutions. *Journal of Materials Science*, **51**, 4627–4638 (2016).  
<https://doi.org/10.1007/s10853-016-9778-x>
- [47] Lou H., Li W., Li C., Wang X.: Systematic investigation on parameters of solution blown micro/nanofibers using response surface methodology based on box-behnken design. *Journal of Applied Polymer Science*, **130**, 1383–1391 (2013).  
<https://doi.org/10.1002/app.39317>
- [48] Dadol G. C., Kilic A., Tijjing L. D., Lim K. J. A., Cabatingan L. K., Tan N. P. B., Stojanovska E., Polat Y.: Solution blow spinning (SBS) and SBS-spun nanofibers: Materials, methods, and applications. *Materials Today Communications*, **25**, 101656 (2020).  
<https://doi.org/10.1016/j.mtcomm.2020.101656>
- [49] Dias F. T. G., Rempel S. P., Agnol L. D., Bianchi O.: The main blow spun polymer systems: Processing conditions and applications. *Journal of Polymer Research*, **27**, 205 (2020).  
<https://doi.org/10.1007/s10965-020-02173-7>
- [50] Ferreira K. N., Oliveira R. R., Castellano L. R., Bonan P. R., Carvalho O. V., Pena L., Souza J. R., Oliveira J. E., Medeiros E. S.: Controlled release and antiviral activity of acyclovir-loaded PLA/PEG nanofibers produced by solution blow spinning. *Biomaterials Advances*, **136**, 212785 (2022).  
<https://doi.org/10.1016/j.bioadv.2022.212785>
- [51] Oliveira J. E., Moraes E. A., Marconcini J. M., Mattoso L. H. C., Glenn G. M., Medeiros E. S.: Properties of poly(lactic acid) and poly(ethylene oxide) solvent polymer mixtures and nanofibers made by solution blow spinning. *Journal of Applied Polymer Science*, **129**, 3672–3681 (2013).  
<https://doi.org/10.1002/app.39061>
- [52] Bang J., Park S., Hwang S-W., Oh J-K., Yeo H., Jin H-J., Kwak H. W.: Biodegradable and hydrophobic nanofibrous membranes produced by solution blow spinning for efficient oil/water separation. *Chemosphere*, **312**, 137240 (2023).  
<https://doi.org/10.1016/j.chemosphere.2022.137240>

- [53] Medeiros E. S., Glenn G. M., Klamczynski A. P., Orts W. J., Mattoso L. H.: Solution blow spinning: A new method to produce micro- and nanofibers from polymer solutions. *Journal of Applied Polymer Science*, **113**, 2322–2330 (2009).  
<https://doi.org/10.1002/app.30275>
- [54] Carlos A. L. M., Mancipe J. M. A., Dias M. L., Thiré R. M. S. M.: Poly(3-hydroxybutyrate-co-3-hydroxyvalerate) core-shell spun fibers produced by solution blow spinning for bioactive agent's encapsulation. *Journal of Applied Polymer Science*, **139**, 52081 (2022).  
<https://doi.org/10.1002/app.52081>
- [55] Souza M. A., Sakamoto K. Y., Mattoso L. H. C.: Release of the diclofenac sodium by nanofibers of poly(3-hydroxybutyrate-co-3-hydroxyvalerate) obtained from electrospinning and solution blow spinning. *Journal of Nanomaterials*, **2014**, 129035 (2014).  
<https://doi.org/10.1155/2014/129035>
- [56] Srinivasan S., Chhatre S. S., Mabry J. M., Cohen R. E., McKinley G. H.: Solution spraying of poly(methyl methacrylate) blends to fabricate microtextured, superoleophobic surfaces. *Polymer*, **52**, 3209–3218 (2011).  
<https://doi.org/10.1016/j.polymer.2011.05.008>
- [57] Gupta P., Elkins C., Long T. E., Wilkes G. L.: Electrospinning of linear homopolymers of poly(methyl methacrylate): Exploring relationships between fiber formation, viscosity, molecular weight and concentration in a good solvent. *Polymer*, **46**, 4799–4810 (2005).  
<https://doi.org/10.1016/j.polymer.2005.04.021>
- [58] Bortolassi A., Guerra V., Aguiar M.: Characterization and evaluate the efficiency of different filter media in removing nanoparticles. *Separation and Purification Technology*, **175**, 79–86 (2017).  
<https://doi.org/10.1016/j.seppur.2016.11.010>
- [59] Sun M., Bloom A. B., Zaman M. H.: Rapid quantification of 3D collagen fiber alignment and fiber intersection correlations with high sensitivity. *PLOS One*, **11**, 157379 (2016).  
<https://doi.org/10.1371/journal.pone.0131814>
- [60] Rezakhaniha R., Agianniotis A., Schrauwen J. T. C., Griffa A., Sage D., Bouten C. V. C., van de Vosse F., Unser M., Stergiopoulos N.: Experimental investigation of collagen waviness and orientation in the arterial adventitia using confocal laser scanning microscopy. *Bio-mechanics and Modeling in Mechanobiology*, **11**, 461–473 (2012).  
<https://doi.org/10.1007/s10237-011-0325-z>
- [61] Tan D. H., Herman P. K., Janakiraman A., Bates F. S., Kumar S., Macosko C. W.: Influence of laval nozzles on the air flow field in melt blowing apparatus. *Chemical Engineering Science*, **80**, 342–348 (2012).  
<https://doi.org/10.1016/j.ces.2012.06.020>
- [62] Tanisali G., Sozak A., Bulut A. S., Sander T. Z., Dogan O., Dağ Ç., Gönen M., Can F., DeMirici H., Ergonul O.: Effectiveness of different types of mask in aerosol dispersion in SARS-CoV-2 infection. *International Journal of Infectious Diseases*, **109**, 310–314 (2021).  
<https://doi.org/10.1016/j.ijid.2021.06.029>
- [63] Žagar E., Kržan A.: SEC-MALS characterization of microbial polyhydroxyalkanoates. *Biomacromolecules*, **5**, 628–636 (2004).  
<https://doi.org/10.1021/bm0300731>
- [64] Rabello L. G., da Conceição Ribeiro R. C.: A novel vermiculite/ vegetable polyurethane resin-composite for thermal insulation eco-brick production. *Composites Part B: Engineering*, **221**, 109035 (2021).  
<https://doi.org/10.1016/j.compositesb.2021.109035>
- [65] Lou H., Han W., Wang X.: Numerical study on the solution blowing annular jet and its correlation with fiber morphology. *Industrial and Engineering Chemistry Research*, **53**, 2830–2838 (2014).  
<https://doi.org/10.1021/ie4037142>
- [66] Atif R., Combrinck M., Khaliq J., Hassanin A. H., Shehata N., Elnabawy E., Shyha I.: Solution blow spinning of high-performance submicron polyvinylidene fluoride fibres: Computational fluid mechanics modeling and experimental results. *Polymers*, **12**, 1140 (2020).  
<https://doi.org/10.3390/polym12051140>
- [67] Wieland M., Arne W., Marheineke N., Wegener R.: Melt-blowing of viscoelastic jets in turbulent airflows: Stochastic modeling and simulation. *Applied Mathematical Modelling*, **76**, 558–577 (2019).  
<https://doi.org/10.1016/j.apm.2019.06.023>
- [68] D'Haene P., Remsen E. E., Asrar J.: Preparation and characterization of a branched bacterial polyester. *Macromolecules*, **32**, 5229–5235 (1999).  
<https://doi.org/10.1021/ma981911k>
- [69] Benavides R. E., Jana S. C., Reneker D. H.: Nanofibers from scalable gas jet process. *ACS Macro Letters*, **1**, 1032–1036 (2012).  
<https://doi.org/10.1021/mz300297g>
- [70] Mossige E., Chandran Suja V., Islamov M., Wheeler S., Fuller G. G.: Evaporation-induced Rayleigh–Taylor instabilities in polymer solutions. *Philosophical Transactions of the Royal Society A*, **378**, 20190533 (2020).  
<https://doi.org/10.1098/rsta.2019.0533>
- [71] Shi L., Wang Y., Zhang Y., Zhuang X., Liu H., Hu Y.: Optimization of the preparation process of electrostatic-solution blow spinning nanofiber yarn using response surface methodology. *Textile Research Journal*, **92**, 4437–4449 (2022).  
<https://doi.org/10.1177/00405175221101179>
- [72] Xu Y., Zou L., Lu H., Chen Z.: Preparation and characterization of electrospun poly(3-hydroxybutyrate-co-3-hydroxyvalerate) fibrous mat. *IOP Conference Series: Materials Science and Engineering*, **87**, 012047 (2015).  
<https://doi.org/10.1088/1757-899X/87/1/012047>
- [73] Mottin A. C., Ayres E., Oréface R. L., Câmara J. J. D.: What changes in poly(3-hydroxybutyrate) (PHB) when processed as electrospun nanofibers or thermo-compression molded film? *Materials Research*, **19**, 57–66 (2016).  
<https://doi.org/10.1590/1980-5373-MR-2015-0280>